

1 Title: Multi-scale Pore-network Representation of Heterogeneous Carbonate Rocks

2 Tannaz Pak^{1,2,*}, Ian B. Butler^{1,2}, Sebastian Geiger^{2,3}, Marinus I.J. van Dijke^{2,3}, Zeyun
3 Jiang^{2,3}, Rodrigo Surmas^{2,3}

4
5 1: School of Geosciences, University of Edinburgh, James Hutton Road, Edinburgh EH9 3FE, UK

6 2: International Centre for Carbonate Reservoirs, West Mains Road, Edinburgh EH9 3JW, UK

7 3: Institute of Petroleum Engineering, Heriot-Watt University, Edinburgh EH14 4AS, UK

8 4: Petrobras Research and Development Centre (Cenpes), Avenida Horácio Macedo, Cidade

9 Universitária, Rio de Janeiro, 21941-915, Brazil

10 *Current address: School of Science and Engineering, Teesside University, Middlesbrough, TS1 3BA,
11 UK., Corresponding author: Tannaz Pak (t.pak@tees.ac.uk)

12

13 Key points:

- 14 • This work investigates the multi-scale porosity of a carbonate rock.
- 15 • We explore representativeness of multi-scale networks by comparing simulated and
16 laboratory measured capillary-pressure vs saturation curves.
- 17 • We present a workflow for selecting number and length scales of networks to
18 generate multi-scale pore-networks.

19

20

21

22 **Abstract:**

23 A multi-scale network integration approach introduced by *Jiang et al.* [2013] is used to
24 generate a representative pore-network for a carbonate rock with a pore-size distribution
25 across several orders of magnitude. We predict the macroscopic flow parameters of the rock
26 utilising i) 3D images captured by X-ray computed micro-tomography and ii) pore-network
27 flow simulations. To capture the multi-scale pore-size distribution of the rock we imaged four
28 different rock samples at different resolutions and integrated the data to produce a pore-
29 network model that combines information at several length-scales that cannot be recovered
30 from a single tomographic image. A workflow for selection of the number and length-scale of
31 the required input networks for the network integration process, as well as fine tuning the
32 model parameters is presented. Mercury injection capillary-pressure data were used to
33 evaluate independently the multi-scale networks. We explore single-scale, two-scale, and
34 three-scale network models and discuss their representativeness by comparing simulated
35 capillary-pressure versus saturation curves with laboratory measurements. We demonstrate
36 that for carbonate rocks with wide pore-size distributions, it may be required to integrate
37 networks extracted from two or three discrete tomographic data sets in order to simulate
38 macroscopic flow parameters.

39 **1. Introduction**

40 Pore-scale fluid flow simulation is a useful tool for calculation of the macroscopic transport
41 properties of porous media, specifically for homogeneous systems [*Meakin and Tartakovsky,*
42 2009; *Joekar-Niasar and Hassanizadeh,* 2012; *Blunt et al.,* 2013; *Wildenschild and*
43 *Sheppard,* 2013]. For complex porous material realistic representation of the pore structure is
44 essential for successful simulations but has proven to be challenging. High-resolution X-ray
45 computed micro-tomography (μ CT) imaging allows detailed study of porous media in 3D
46 (reviews by *Wildenschild and Sheppard* [2013], *Fusseis et al.* [2014], and *Bultreys et al.*
47 [2016]). Reliable application of this technique requires sufficient image quality to allow
48 discrimination of the important features of the sample. Pore-network models (PNM) extracted
49 from binarised μ CT images (see review by *Dong* [2007]) are simple representations of pore

50 structures to simulate flow at a reduced computational cost. Although appealing, PNM
51 predictions often do not agree well with the corresponding laboratory measurements,
52 specifically for complex pore systems such as carbonate rocks [Sorbie and Skauge, 2012].
53 The trade-off between the sample size and μ CT image resolution means that a single μ CT
54 volume may not capture the details of a multi-scale pore structure [Hebert et al., 2014].
55 Capturing a representative image of heterogeneous samples with pore-size distribution (PSD)
56 spanning several orders of magnitude is an outstanding challenge with existing μ CT
57 instrumentation. A representative elementary volume (REV) is required that is the smallest
58 sample to which measured properties of the bulk sample can be assigned [Bear, 1972].
59 Generating two-scale PNM that are representative of complex pore systems has been studied
60 by Biswal et al. [2007]; Biswal et al. [2009] and Ghous et al. [2008], and more recently by
61 Prodanović et al. [2015], Mehmani and Prodanović [2014], and Bultreys et al. [2015].
62 Jiang et al. [2013] introduced a network integration method to generate PNMs of arbitrarily
63 large volumes that can incorporate multi-scale pore systems extracted [Jiang et al., 2007]
64 from images captured at different resolutions. A detailed PNM extracted from a high
65 resolution μ CT volume (fine-network) is combined with a network extracted from a coarse
66 resolution volume (coarse-network). For details of how the nodes/bonds of the differently
67 scaled models are interconnected see Jiang et al. [2013]. The domain of the fine-network is
68 smaller than that of the coarse-network, hence a larger network that is statistically equivalent
69 to the fine-network is generated and then integrated into the coarse-network. The generated
70 multi-scale networks can be heavier than the original fine-network, with an adverse effect on
71 the computational cost of fluid flow simulations. To address this Jiang et al. [2013], reduced
72 the number of fine-network elements by a fraction (f_F) such that $0 < f_F \leq 1$. It is also possible to
73 scale the size of the domain of the two-scale network (nesting-domain) with respect to that of

74 the original coarse image using a scaling factor (δ) that is arbitrary but is restricted by the
75 available computational power for flow simulations.

76 We investigate generation of a representative PNM for a dolomite using *Jiang et al.* [2013]’s
77 approach and a quasi-static pore-network flow simulator [*Ryazanov et al.* [2009]]. We
78 evaluate *Jiang et al.* [2013]’s approach by comparing simulated $P_c(S)$ curves with those
79 measured experimentally using mercury injection capillary-pressure (MICP) tests. A
80 workflow is proposed for multi-scale network generation to address (i) the choice of sample
81 size and, hence, image resolution, and (ii) the tuning of model parameters to reproduce the
82 laboratory $P_c(S)$ curves.

83 **2. Imaging and Mercury Porosimetry**

84 A sucrosic dolomite (Silurian Dolomite (SD), Thornton formation, Chicago, Illinois, US)
85 with pore sizes spanning 3 orders of magnitude was used (Figure 1). Laboratory
86 measurements of a 38mm diameter core displayed porosity and permeability of 17% and
87 ~ 50 mD, respectively (Figure 1b).

88 We imaged, using μ CT, four samples of diameter $D=2, 5, 25$ and 38mm, at resolutions of 2.3,
89 12, 21 and 32.8 μ m, respectively (Figure 1b). Both the image voxel sizes and the corrected
90 image resolutions are reported in Table 1, the correction accounts for the unsharpness caused
91 by the X-ray source spot size [*Feser et al.*, 2008]. The values presented throughout the rest of
92 the manuscript are the corrected image resolution values. As currently worded, this is still a
93 bit unclear. Methods are detailed in the SI and *Pak et al.* [2013]. Sizes were selected because
94 38mm is a standard petrophysical plug, 25mm is the largest sample the MICP could analyse,
95 and 5mm and 2mm provide details of the finer porosity. Figure 1c displays the PSD derived
96 from these four data volumes (Figure 1b) using a sphere fitting method [*Jiang et al.*, 2007].
97 Each volume has captured only a portion of the PSD. In SD recrystallization to dolomite has
98 produced a structure in which the pores are lined by the apices and edges of dolomite rhombs

99 with well sorted crystals sizes. Microscope images (Figure S1.) show that smaller pores are
100 formed in between a few crystals, are uniformly present throughout the sample, suggesting
101 little or no spatial correlation of the micro-porosity. Hence, we uniformly integrate the fine-
102 network in the entire nesting-domain.

103 MICP measurement was performed on three 25 mm diameter SD core plugs imaged at
104 resolution 21 μ m (Figure S2). MICP provides $P_c(S)$ curves from which pore-throat size
105 distribution can be extracted [*Ritter and Drake, 1945*]. The MICP-based porosity for these
106 samples is 18.03, 16.03 and 18.1%. The image-based porosities at this resolution are 8.05,
107 6.03 and 8.12%, respectively, hence the 21 μ m represent a coarse-scale resolution.

108 **3. Multi-scale PNM Reconstruction**

109 We explore representing the SD pore structure using multi-scale networks to incorporate
110 features extracted from the four μ CT volumes shown in Figure 1b. For 3D renderings of
111 these networks see Figure S3. The physical size of these networks can be found from the
112 image dimensions and voxel resolutions (Table 1). The two coarse-scale networks are
113 globally disconnected while the fine-scale networks are connected with simulated absolute
114 permeability $k_{abs} > 0$ mD. The total (and connected) porosity shows an increasing trend with
115 resolution enhancement, as does the calculated permeability. The two fine-networks display
116 calculated permeability values higher than the laboratory measurement i.e. 50 mD. The small
117 samples do not contain a REV and the calculated permeability values reflect the local
118 connectivity of the pore system at these scales. However, even for the 2.3 μ m resolution
119 network about 11% of the pore volume is disconnected, reflecting that the resolution is
120 insufficient to capture the smallest pore-throats, or that isolated pores exist in the sample.

121 **3.1. Two-scale PNMs**

122 Six possible combinations for generating two-scale networks are 32.8-21 μ m, 32.8-12 μ m,
123 32.8-2.3 μ m, 21-12 μ m, 21-2.3 μ m, and 12-2.3 μ m, referring to image resolution. Essentially,
124 we need (i) a sufficiently large coarse-network that represents the largest pores, (ii) a fine-
125 network with sufficient resolution that captures the smaller pores, and (iii) a sufficient
126 overlap of the PSD of the two networks to ensure representation of the intermediate-size
127 pores. Hence, 12-2.3 μ m and 32.8-21 μ m combinations are not acceptable. In what follows
128 other combination are discussed.

129 **3.1.1. Combination of 21 and 2.3 μ m PNMs**

130 Figure 2a shows ten networks extracted from sub-domains ($\delta=0.1-1$) of the 21 μ m coarse-
131 network. At $\delta=0.4$ the domain is sufficiently large to accommodate a cluster of large pores,

132 hence the network porosity displays a sharp increase, Figure 2b. At $\delta=0.5$ the domain
133 accommodates a connected cluster of pores, therefore, $k_{abs}>0$. However, as the sub-domain
134 grows ($\delta>0.5$) the networks become again disconnected, suggesting that only a locally
135 connected cluster is captured at $\delta=0.5$ which is not representative of the connectivity of larger
136 pores at this scale.

137 Figure 2c displays the sensitivity of these two-scale networks to f_F . Porosity increases linearly
138 with the inclusion of increasing fractions of the fine-network, while the permeability starts to
139 converge for $f_F>0.05$. Thus even a reduced version of a fine-network can provide the required
140 connectivity to two-scale network.

141 The calculated porosity and permeability display convergence at $\delta>0.6$ (i.e. total porosity
142 $\sim 6\%$ and $k_{abs}=0$). Figure 2d, however, shows that the $P_c(S)$ curves, calculated using these
143 two-scale PNMs ($f_F=0.01$, $0.6<\delta<1$), do not converge. The curves display jumps at different
144 saturations depending on the nesting-domain size. Examination of Figure 2a reveals that the
145 coarse-network contains two connected clusters of elements (pores and nodes) that are
146 disconnected from each other. Network integration provides connectivity between these
147 clusters through elements of the fine-network. Cluster 1 is connected to the inlet and can be
148 invaded by the injected phase directly. Cluster 2 is only accessible through cluster 1 using the
149 fine-network connections. The jump occurs at saturation S^* that is equal to the ratio of the
150 volume of cluster 1 to the total volume of the connected pore space.

151 As δ increases, cluster 2 grows more significantly compared to cluster 1, hence S^* approaches
152 0.8. Hence, the selected domain from the $21\mu\text{m}$ resolution image does not contain a REV.
153 However, the MICP core plugs were approximately 60% larger than the box selected for
154 pore-network simulations, and the MICP-driven $P_c(S)$ curves for three 25mm diameter SD
155 plugs are very close (Figure S2a), this suggests that the MICP plugs themselves are
156 representative for this rock.

157

3.1.2. Combination of 32.8 and 2.3 μ m PNMs

158 For this combination the two-scale network porosity converges for $\delta > 0.6$ (Figure 3a) while
159 $k_{abs} = 0$ for all sub-domains. Further, the simulated $P_c(S)$ curves for this combination ($f_F = 0.01$)
160 also converge for $\delta > 0.6$ (Figure 3b). This indicates that sub-domains of the 38.2 μ m image
161 with $\delta > 0.6$ contain a REV of SD. The $P_c(S)$ curves, however, show a jump at $S_{air} \sim 0.8$ causing
162 an overestimation of the experimental capillary-pressure values for $S_{air} < 0.8$. The PSD of the
163 2.3 μ m network (Figure 1b) shows a peak at $\sim 6\mu$ m, while pores larger than 10 μ m display less
164 than 20% probability (i.e. volume fraction). Since the coarse-network is globally
165 disconnected, the two-scale networks are connected only through fine-network elements. The
166 initial displacement ($S_{air} > 0.8$) corresponds to the pores accessible from the inlet. At $S_{air} \sim 0.8$
167 the pressure needs to increase sufficiently before elements from the fine-network can be
168 invaded. For the converged set of $P_c(S)$ curves, on Figure 3b, the f_F is equal to 0.01. Including
169 a larger f_F suppresses the jump in the capillary-pressure curve but does not totally remove it.
170 The $P_c(S)$ curve for the $\delta = 0.6$ and $f_F = 0.04$ network shows a small jump at $S_{air} = 0.8$ from
171 $\sim 21kP$ to $\sim 47kP$ corresponding to invasion of pore-throats with radius of 40 μ m to 16 μ m.
172 However, this size range is insufficiently represented in both 32.8 and 2.3 μ m networks. In
173 particular, a small f_F makes a reduced network less representative of the two ends of the PSD.
174 In practice, the difference in the domain sizes of the coarse and fine-networks causes higher
175 f_F values to make the two-scale network substantially more computationally expensive.

176

3.1.3. Combination of 32.8 and 12 μ m PNMs

177 For this combination the calculated $P_c(S)$ curves show a good match with the laboratory
178 measurements at $S_{air} > 0.04$ (Figure 4). However, the simulations stop at capillary-pressure
179 values around 276kP, due to fine-network resolution limitations. Using a higher resolution

180 fine-network may not provide significant additional connectivity, but may prove essential for
181 calculation of saturation values.

182 **3.2.Three-scale PNMs**

183 We have demonstrated that a finer length-scale needs to be integrated into the 32.8–12 μm
184 combination, or an intermediate length-scale must be added to the 32.8–2.3 μm combination.

185 To integrate three PNMs of different length-scales first the two smaller networks are
186 integrated into a two-scale network that is subsequently integrated into the largest scale
187 network. This involves selecting two sets of δ and f_F . As the number of length-scales
188 increases, sensitivity analysis on the effect of δ and f_F becomes increasingly time consuming.

189 Figure 5 compares the closest simulated three-scale network $P_c(S)$ curve with the laboratory
190 measurement. This three-scale PNM is generated by integration of the 2.3 and 12 μm
191 networks ($\delta=1, f_F=0.004$) followed by integration of that network with the 32.8 μm network
192 ($\delta=0.7, f_F=0.006$). The nesting-domain sizes for the 2.3 and 12 μm networks are close, hence
193 selecting $\delta=1$ is feasible. To keep the three-scale network computationally manageable while
194 ensuring representativity, we selected $\delta=0.7$ for the second step.

195 Sensitivity analysis was performed on the value of f_F within the range of 0.001 to 0.1 for the
196 first step and 0.001 to 0.006 for the second step. The calculated $P_c(S)$ curves show that
197 keeping the first f_F value at 0.004 enables the inclusion of a sufficient number of elements
198 from the 2.3 μm network for simulations to predict the higher capillary-pressures while
199 eliminating artificial jumps in capillary-pressure.

200 We analysed the goodness of fit for the $P_c(S)$ curves for the single (at 2.3 μm and 12 μm), two-
201 scale, and three-scale PNMs using the Chi-squared measure. Single-scale networks yield the
202 poorest capillary-pressure predictions while the three-scale network and the two-scale (32.8-
203 12 μm) show only minor deviations from the laboratory measurements (Figure 5). Chi-
204 squared for the 32.8-12 μm network is marginally better than that of the 32.8-12-2.3 μm network,

205 since the Chi-squared test only compares model predictions against the laboratory
206 measurements, but does not capture that the model does not predict capillary-pressures at low
207 saturations for the 32.8-12 μ m combination.

208 Although the calculated absolute permeability values (Table 2) do not accurately match the
209 experimental observation (50mD), the calculated values are close and within the same order
210 of magnitude. The deviation could stem from (i) the fact that the simulations are conducted
211 on a subsection of the acquired μ CT images, (ii) errors introduced in noise filtering and
212 subsequent segmentation steps, and (iii) image properties, in particular, the partial volume
213 effect. This can cause features (e.g. pore-throats) smaller than one voxel to appear as large as
214 a voxel in the segmented images. Larger pore-throats display less resistance to the flow and
215 hence a higher absolute permeability is calculated.

216 No laboratory $kr(S)$ measurements were available, hence simulated $kr(S)$ curves for single
217 and multi-scale PNMs are compared in SI. In summary, we show that the parameters
218 involved in the network integration, as well as the number and resolution of the input single-
219 scale networks can have a substantial impact on the shape of the $kr(S)$ curves calculated
220 based on the multi-scale PNMs. Future studies could aim to compare the calculated $kr(S)$
221 curves with laboratory measurements to establish the effect of network integration on
222 predicting $kr(S)$ curves.

223 **4. Multi-scale Network Generation Workflow**

224 Figure 6 is a practical guide for selection of length-scales for generating a multi-scale PNM
225 from μ CT data and is additionally informed by thin-section imaging and MICP techniques.
226 This information assists sample size selection, the choice of length-scales, and resolutions for
227 multi-scale network generation.

228 **5. Summary and Conclusions**

229 A network integration approach introduced by *Jiang et al.* [2013] is used to generate
230 representative models for a dolomite with multi-scale porosity. PNMs extracted from μ CT
231 images acquired at different length-scales are integrated into single multi-scale PNMs
232 incorporating all the porosity features that exist in the rock. The main contribution of this
233 paper is to present a workflow for effective selection of appropriate length-scales for
234 generation of the multi-scale network. The choice of images to be combined is informed by
235 MICP throat-size distributions. Additionally, there are two free parameters (δ and f_F) in the
236 model. The integrated networks are used to reproduce $P_c(S)$ curves, evaluated against MICP
237 laboratory measurements. We demonstrate that $P_c(S)$ curves calculated based on the two-
238 scale and three-scale PNMs provide significantly closer comparisons to the laboratory
239 measurements compared to a single-scale network model. Future studies need to validate
240 calculated $kr(S)$ curves against experimental measurements to optimise multi-scale network
241 generation for predictions of multiphase fluid behaviour.

242 **Acknowledgement:**

243 We would like to thank Petrobras and BG Group for their sponsorship of the ICCR
244 programme and the permission to publish this work from the project SatuTrack. We thank
245 Petrobras Research Centre for the mercury injection capillary-pressure tests, Mike Hall for
246 preparing the thin-sections, and the Centre of Environmental Scanning Microscopy at Heriot-
247 Watt University. All data for this paper is properly cited and referred to in the reference list.
248 Simulations were carried out with the PAT software developed at Heriot-Watt University.
249 Input data and software used in this paper can be obtained from the authors upon request.

250 **References:**

251 Bear, J. (1972), *Dynamics of Fluids in Porous Media*, Elsevier, New York.

252 Biswal, B., P. Øren, R. Held, S. Bakke, and R. Hilfer (2007), Stochastic multiscale model for
253 carbonate rocks, *Phys. Rev. E: Stat., Nonlinear, Soft Matter Phys.*, 75(6), 061303.

254 Biswal, B., P. Øren, R. J. Held, S. Bakke, and R. Hilfer (2009), Modeling of multiscale
255 porous media, *Image Analysis and Stereology*, 28, 23-34.

256 Blunt, M. J., B. Bijeljic, H. Dong, O. Gharbi, S. Iglauer, P. Mostaghimi, A. Paluszny, and C.
257 Pentland (2013), Pore-scale imaging and modelling, *Adv. Water Resour.*, 51, 197-216.

258 Bultreys, T., L. Van Hoorebeke, and V. Cnudde (2015), Multi-scale, micro-computed
259 tomography-based pore network models to simulate drainage in heterogeneous rocks, *Adv.*
260 *Water Resour.*, 78, 36-49.

261 Bultreys, T., W. De Boever, and V. Cnudde (2016), Imaging and image-based fluid transport
262 modeling at the pore scale in geological materials: A practical introduction to the current
263 state-of-the-art, *Earth-Science Reviews*, 155, 93-128.

264 Dong, H. (2007), *Micro-CT imaging and pore network extraction*.

265 Feser, M., J. Gelb, H. Chang, H. Cui, F. Duerwer, S. Lau, A. Tkachuk, and W. Yun (2008),
266 Sub-micron resolution CT for failure analysis and process development, *Measurement*
267 *science and technology*, 19(9), 094001.

268 Fusses, F., X. Xiao, C. Schrank, and F. De Carlo (2014), A brief guide to synchrotron
269 radiation-based microtomography in (structural) geology and rock mechanics, *Journal of*
270 *Structural Geology*, 65, 1-16.

271 Ghous, A., et al. (2008), 3D Imaging of Reservoir Core at Multiple Scales; Correlations to
272 Petrophysical Properties and Pore Scale Fluid Distributions, edited, International Petroleum
273 Technology Conference.

274 Hebert, V., C. Garing, L. Luquot, P. A. Pezard, and P. Gouze (2014), Multi-scale X-ray
275 tomography analysis of carbonate porosity, *Fundamental Controls on Fluid Flow in*
276 *Carbonates: Current Workflows to Emerging Technologies*. Geological Society, London,
277 *Special Publications*, 406.

278 Jiang, Z., M. Dijke, K. Sorbie, and G. Couples (2013), Representation of multiscale
279 heterogeneity via multiscale pore networks, *Water Resour. Res.*, 49(9), 5437-5449.

280 Jiang, Z., K. Wu, G. Couples, M. Van Dijke, K. Sorbie, and J. Ma (2007), Efficient extraction
281 of networks from three-dimensional porous media, *Water Resour. Res.*, 43(12).

282 Joekar-Niasar, V., and S. Hassanizadeh (2012), Analysis of fundamentals of two-phase flow
283 in porous media using dynamic pore-network models: A review, *Critical Reviews in*
284 *Environmental Science and Technology*, 42(18), 1895-1976.

285 Meakin, P., and A. M. Tartakovsky (2009), Modeling and simulation of pore-scale
286 multiphase fluid flow and reactive transport in fractured and porous media, *Rev. Geophys.*,
287 47(3), RG3002.

288 Mehmani, A., and M. Prodanović (2014), The effect of microporosity on transport properties
289 in porous media, *Adv. Water Resour.*, 63, 104-119.

290 Pak, T., S. Geiger, Z. Jiang, K. S. Sorbie, S. Elphick, M. I. J. van Dijke, and I. Butler (2013),
291 Pore-Scale Visualisation of Two-Phase Fluid Displacement Processes in a Carbonate Rock
292 using X-ray micro-Tomography Technique, in *SPE Reservoir Characterization and*
293 *Simulation Conference and Exhibition*, edited, Society of Petroleum Engineers, Abu Dhabi,
294 UAE.

295 Prodanović, M., A. Mehmani, and A. P. Sheppard (2015), Imaged-based multiscale network
296 modelling of microporosity in carbonates, *Geological Society, London, Special Publications*,
297 406(1), 95-113.

298 Ritter, H., and L. Drake (1945), Pressure porosimeter and determination of complete
299 macropore-size distributions. Pressure porosimeter and determination of complete

300 macropore-size distributions, *Industrial & Engineering Chemistry Analytical Edition*, 17(12),
 301 782-786.
 302 Ryazanov, A. V., M. I. J. van Dijke, and K. S. Sorbie (2009), Two-Phase Pore-Network
 303 Modelling: Existence of Oil Layers During Water Invasion, *Transp. Porous Media*, 80(1),
 304 79-99.
 305 Sorbie, K., and A. Skauge (2012), Can network modeling predict two-phase flow functions?,
 306 *Petrophysics*, 53(06), 401-409.
 307 Wildenschild, D., and A. P. Sheppard (2013), X-ray imaging and analysis techniques for
 308 quantifying pore-scale structure and processes in subsurface porous medium systems, *Adv.*
 309 *Water Resour.*, 51(0), 217-246.

310 Nomenclature Table:

S	saturation
S^*	the saturation at which the jump occurs
S_{air}	air saturation
f_F	Fraction of fine network
δ	Nesting-domain fraction
$P_c(S)$	relative permeability
$k_r(S)$	relative permeability
$k_{rnw}(S)$	non-wetting phase relative permeability
$k_{rw}(S)$	wetting phase relative permeability
k_{abs}	absolute permeability
r	radius
χ^2	Chi-squared

311 Tables:

312 **Table 1: Network parameters for PNM shown in Figure S3.**

Image Resolution (μm), corrected for spot size	Voxel Size (μm)	Domain Dimensions (voxels)	Number of Nodes	Number of Bonds	Connected Porosity %	Total imaged Porosity %	k_{abs} (mD)

32.8	32	881×901×901	10318	12736	0	3.52	0
21	21	821×860×720	19897	24093	0	6.03	0
12	5	500×500×500	3418	4127	6.15	9.23	75.63
2.3	2	570×450×380	1733	2089	12.72	14.32	99.75

313

314 **Table 2: Network parameters for multi-scale PNMs**

Image Resolution (μm)	Number of Nodes	Number of Bonds	Connected Porosity %	Total Porosity %	k_{abs} (mD)	Average coordination number
32.8-12-2.3	13956	22954	3.81	3.96	128.14	3.44
32.8-2.3	439131	534791	3.31	3.36	178.02	3.02
32.8-12	76916	100743	4.28	4.43	90.55	2.94

315

316 **Figure Captions:**

317 **Figure 1: (a) Backscattered SEM image of a polished thin-section of SD in three different magnifications,**
318 **acquired at SEM facility at Heriot-Watt University (resolution $\sim 0.7\mu\text{m}$). The left hand side image**
319 **represents a tessellated image constructed from 400 fields of view stitched together, (b) Four μCT images**
320 **of SD rock samples ($D=2, 5, 25$ and 38mm) captured at respective resolutions of $2.3, 12, 21$ and $32.8\mu\text{m}$.**
321 **The scanned samples were not generated sequentially by cutting the same core, (c) PSD derived from the**
322 **four images shown in (b) using a sphere fitting method [Jiang et al., 2007].**

323 **Figure 2: (a) Networks extracted from ten sub-domains with δ ranging from 0.1 to 1 for the coarse-**
324 **network (resolution $21\mu\text{m}$), blue colour shows connected pink is globally disconnected elements, (b) Static**
325 **properties of the sub-domain networks shown in (a), the blue box corresponds to the jump in the total**
326 **porosity captured for $\delta=0.4$ while the red box shows the locally connected cluster captured in the sub-**
327 **domain with $\delta=0.5$, (c) Effect of fraction of fine-network (f_F) on porosity and permeability of two-scale**
328 **networks with $\delta=0.7$ (see 3D renderings in Figure S4), and (d) Effect of nesting-domain size on the two-**
329 **scale (21 and $2.3\mu\text{m}$, $f_F=0.01$) $P_c(S)$ curves in comparison with laboratory measurements.**

330 **Figure 3: (a) The porosity of the sub-domains of the $32.8\mu\text{m}$ network as a function of the domain fraction,**
331 **(b) The $P_c(S)$ curves for the combined $32.8 - 2.3\mu\text{m}$ networks compared with the MICP laboratory**
332 **measurements. The $32.8\mu\text{m}$ network becomes sufficiently representative for $\delta>0.6$ displaying converged**
333 **porosity and $P_c(S)$ curves. δ : Nesting-domain fraction, f_F : Fraction of fine-network.**

334 **Figure 4: The $P_c(S)$ curves for the two-scale 32.8–12 μm ($\delta=0.7$) network for various f_F . The model**
335 **predictions show a good fit to the experimental data, however, the model does not predict the higher**
336 **pressure end of the curve.**

337 **Figure 5: The $P_c(S)$ curves for the three-scale network compared with the laboratory data, two-scale and**
338 **single-scale simulations. The plot also shows the Chi-squared (χ^2) measure for these networks. The three-**
339 **scale network model displays the best fit to the MICP data.**

340 **Figure 6: Multi-scale network generation workflow and tuning.**

341

Figure 1. Figure

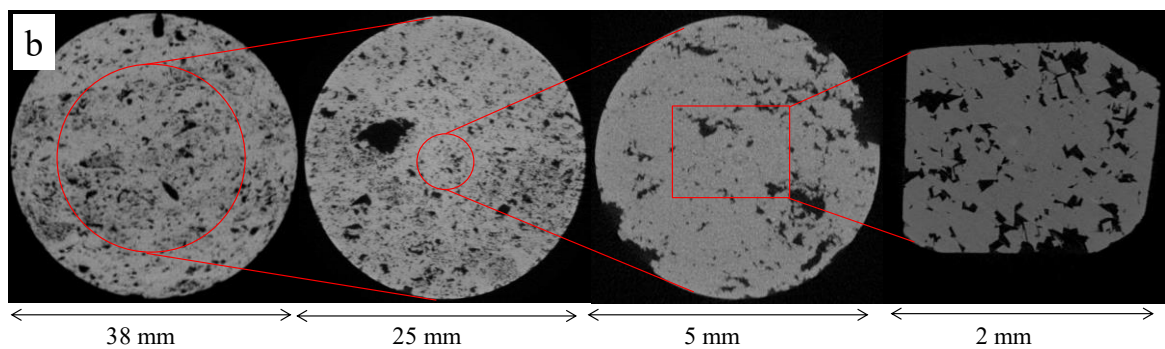
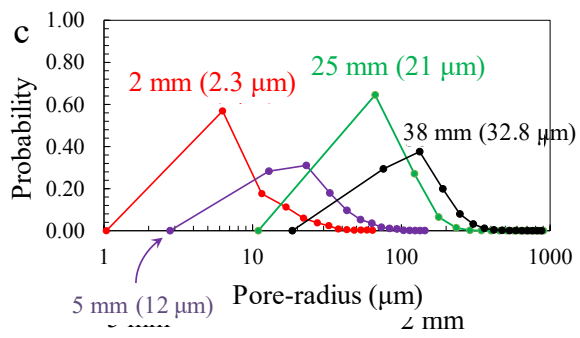
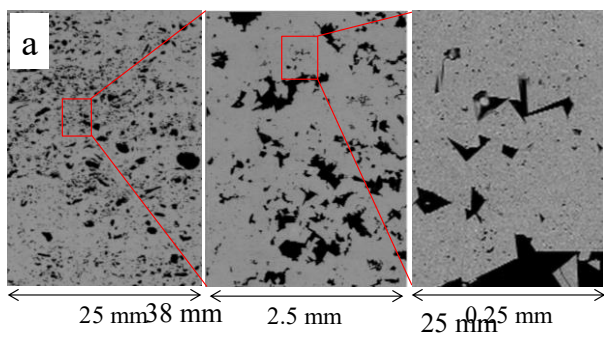


Figure 2. Figure

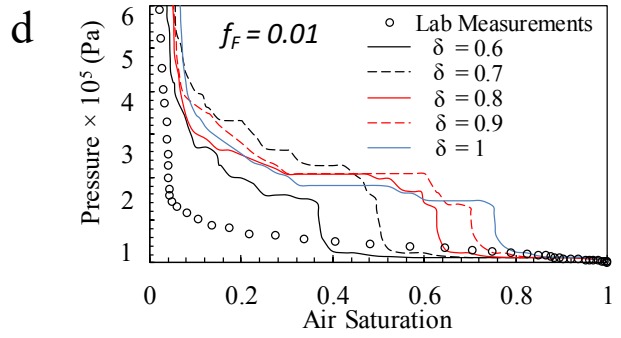
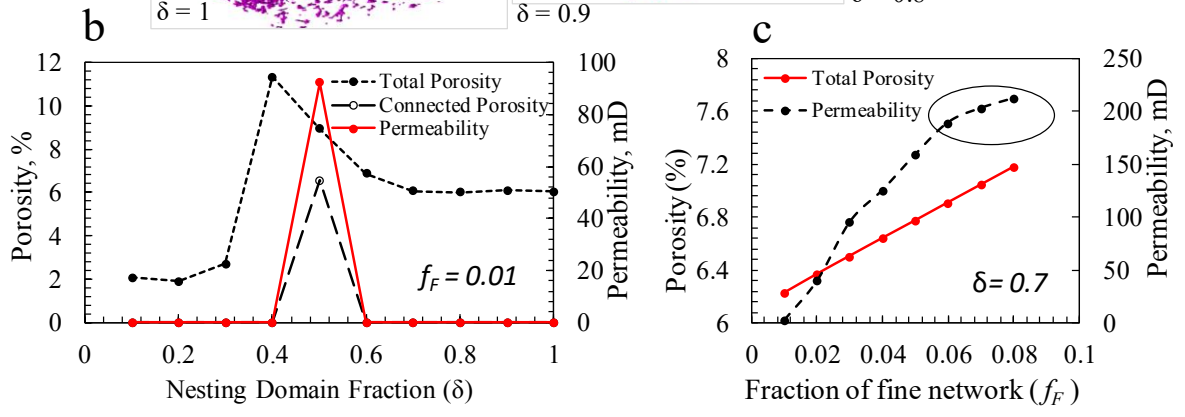
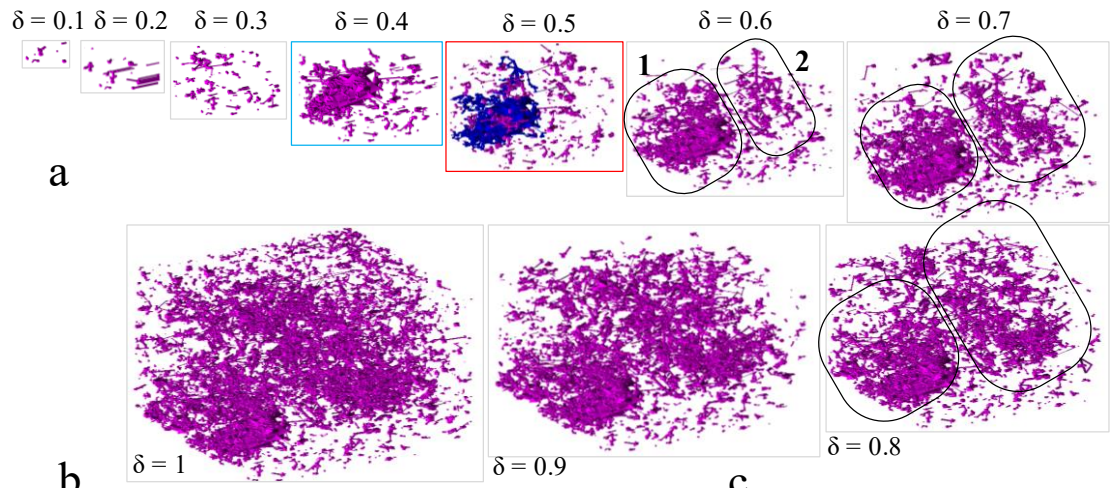


Figure 3. Figure

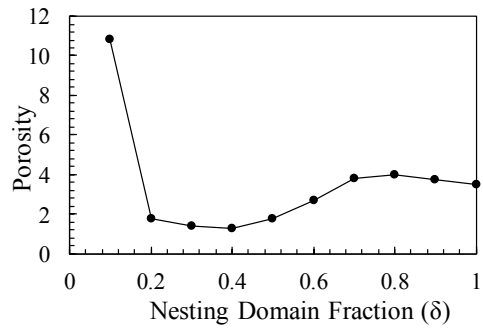
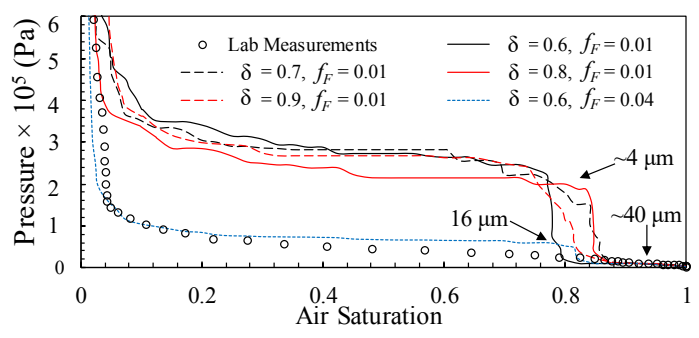
a**b**

Figure 4. Figure

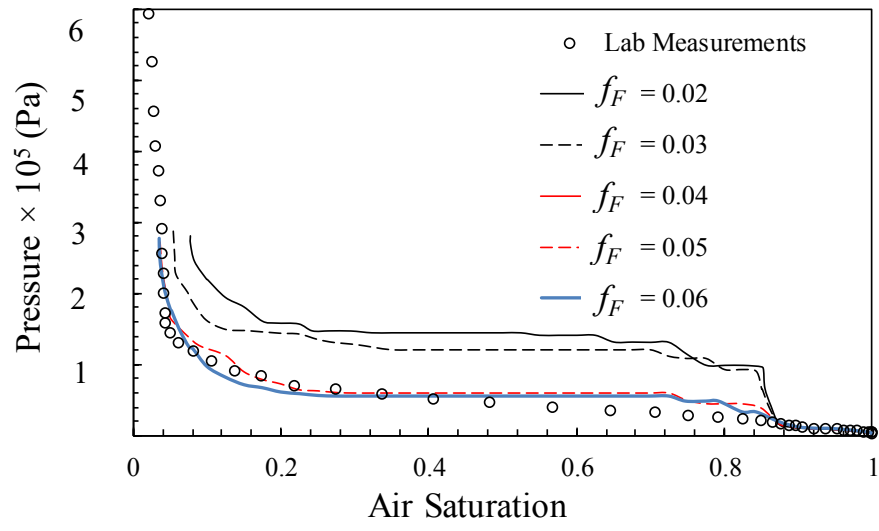


Figure 5. Figure

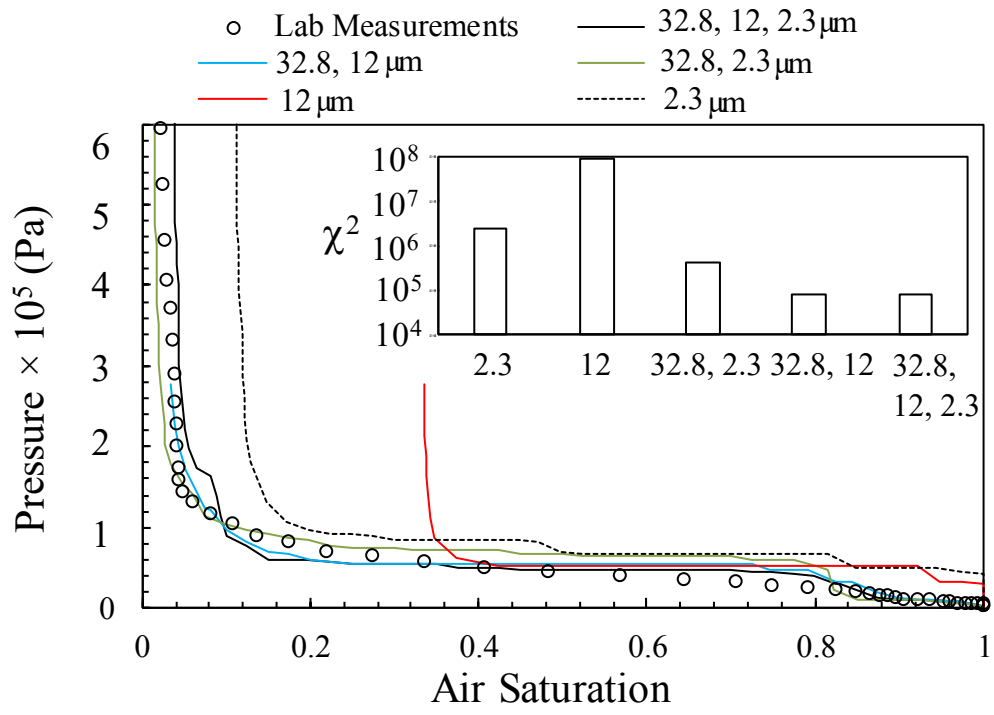
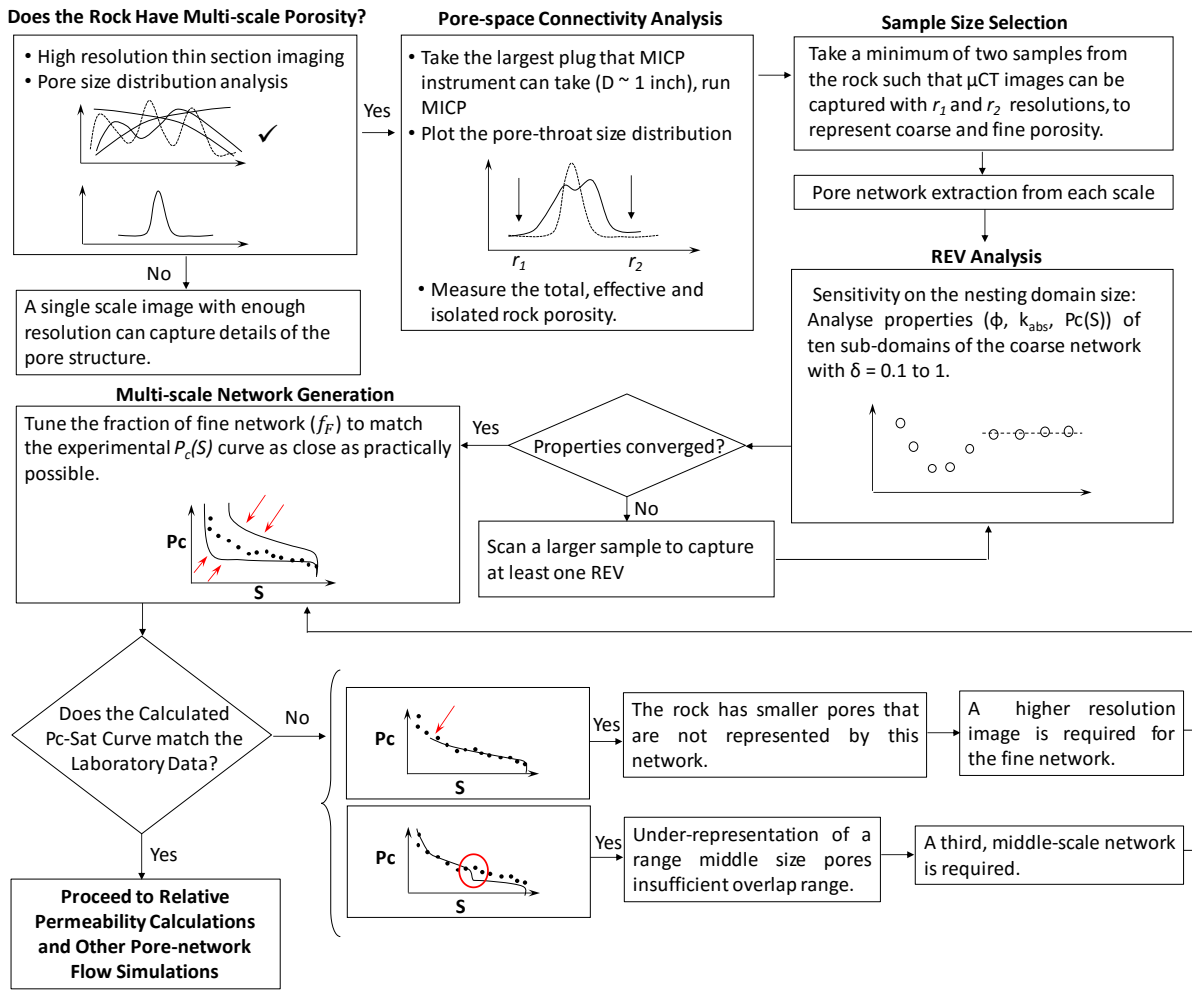


Figure 6. Figure

Multi-scale Network Generation Workflow



Multi-scale Pore Network Representation of Heterogeneous Carbonate Rocks

Tannaz Pak^{1, 2, *}, Ian B. Butler^{1, 2}, Sebastian Geiger^{2, 3}, Marinus I.J. van Dijke^{2, 3}, Zeyun Jiang^{2, 3}, Rodrigo Surmas^{2, 3}

1: School of Geosciences, University of Edinburgh, James Hutton Road, Edinburgh EH9 3FE, UK

2: International Centre for Carbonate Reservoirs, West Mains Road, Edinburgh EH9 3JW, UK

3: Institute of Petroleum Engineering, Heriot-Watt University, Edinburgh EH14 4AS, UK

4: Petrobras Research and Development Centre (Cenpes), Avenida Horácio Macedo, Cidade Universitária, Rio de Janeiro, 21941-915, Brazil

*Current address: School of Science and Engineering, Teesside University, Middlesbrough, TS1 3BA, UK.

Corresponding author: Tannaz Pak (t.pak@tees.ac.uk)

Contents of this file

- Figures S1 to S5
- Methodological details
- A comparison of simulated $kr(S)$ curves for single or multi-scale pore-networks.

Introduction

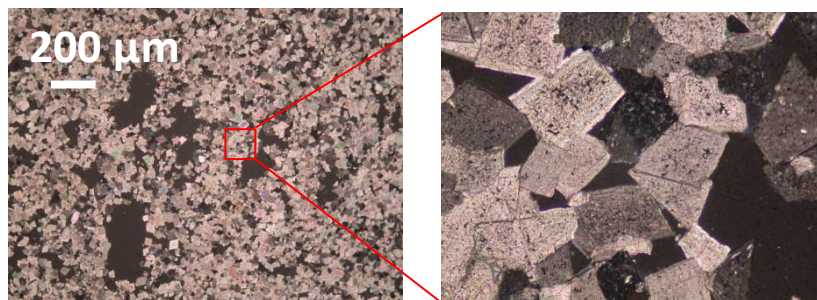


Figure S1: Microscope images for SD showing well sorted crystal sizes and uniform spread of the finer porosity in the rock.

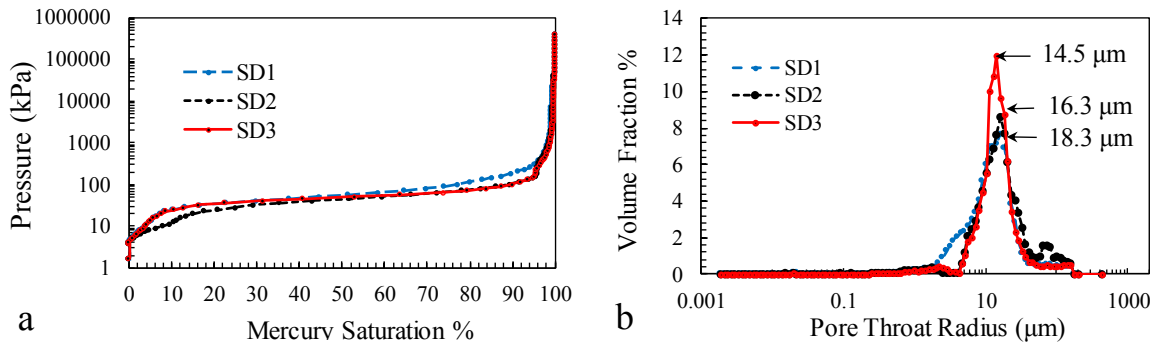


Figure S2: (a) $P_c(S)$ curve for three SD plugs ($D = 25$ mm) from which pore-throat size distributions (b) are extracted .

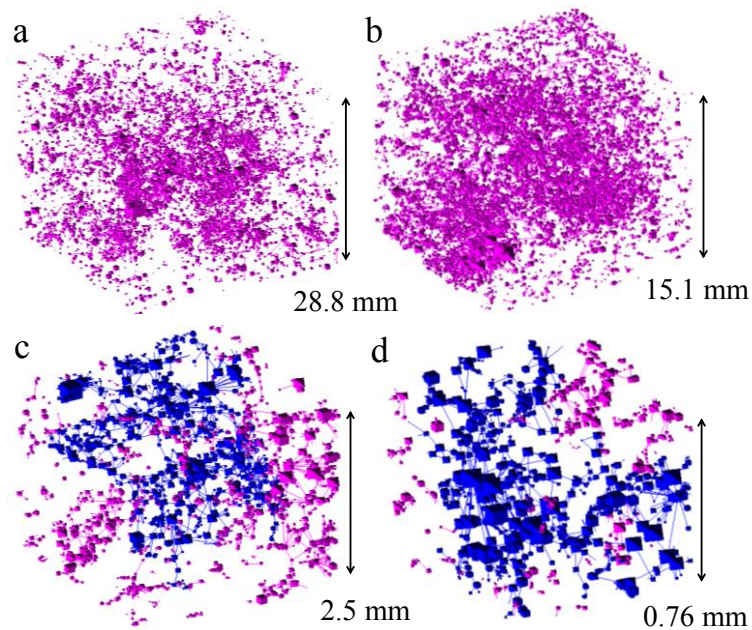


Figure S3: Pore-networks extracted from the four μ CT images of the SD samples shown in Figure 3c. Pink and blue indicate the disconnected and connected elements, respectively. See Table 1 for more properties of these four networks.

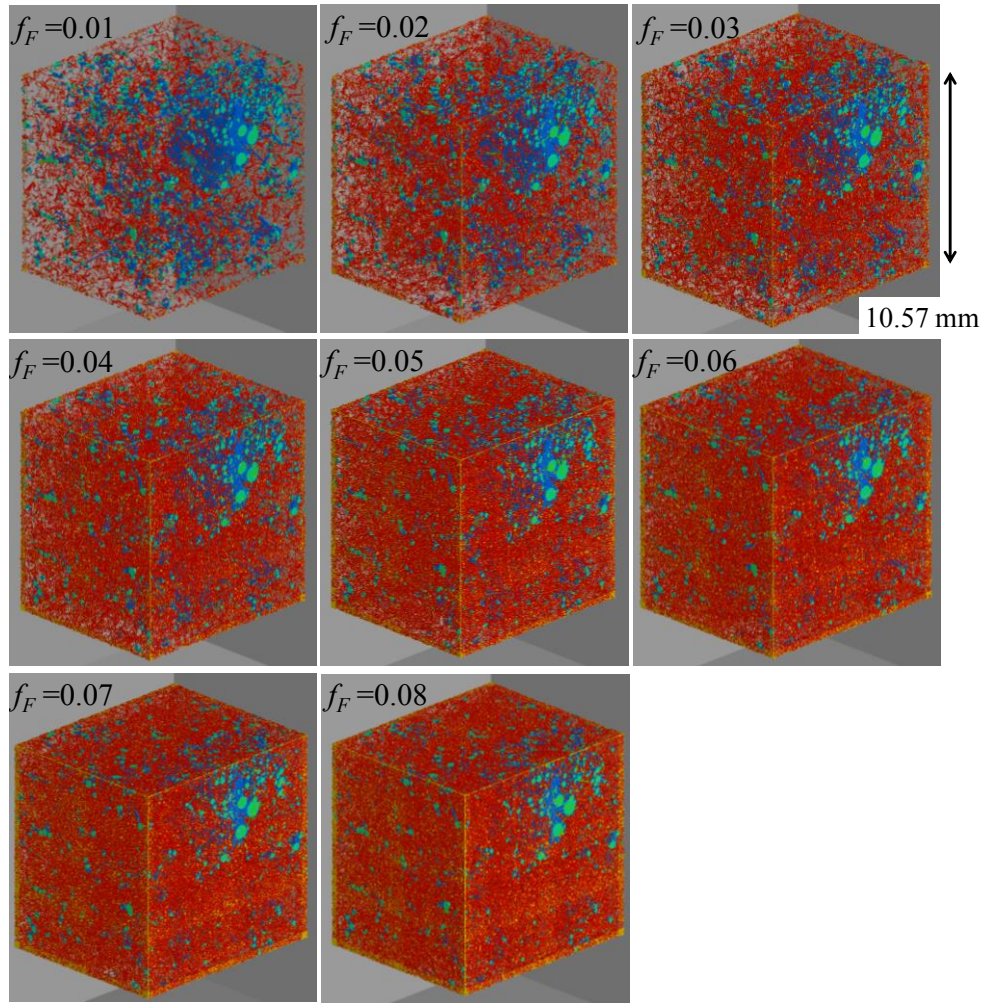


Figure S4: 3D renderings of the two-scale networks with $\delta = 0.7$ and $0.01 \leq f_F \leq 0.08$. Blue/green shows the coarse-network elements and red shows the fine-network elements.

Methodological Details

X-ray μ CT imaging was performed using a μ CT instrument built in-house at the University of Edinburgh with a cone-beam configuration. Data were reconstructed using Octopus v 8.5 and processed using Avizo-Fire (v8). Images were filtered using an anisotropic diffusion filter, and segmented using the watershed segmentation method.

Simulation of Relative Permeability Curves

Comparison of experimental $kr(S)$ curves and model predictions for complex (multi-scale) pore structures has not been addressed in many publications (as an example see *Bultreys et al. [2015]*) mainly because of (i) limited availability of experimental data, and (ii) the challenging nature of generating pore-networks that are representative of complex porous media at the scale at which the experiment was performed. What is most commonly reported is the comparison

of simulated $kr(S)$ curves for single or multi-scale pore-networks with a range of the model inputs. For instance, *Prodanović et al. [2015]*. compared the $kr(S)$ curves calculated based on single-scale and two-scale pore-network models and explained the curves display a shift in cross-over point saturation as a result of including micro-porosity. No laboratory $kr(S)$ measurements were available to this research. Therefore, only calculated $kr(S)$ curves based on two-scale and three-scale networks are compared here, (Figure S5). The $kr(S)$ curves are calculated for a drainage process, here we use mercury invading a fully air saturated network. The curve calculated for the mercury/air system can be modified to generate oil/brine curves, by accounting for the difference in the interfacial tension and contact angles.

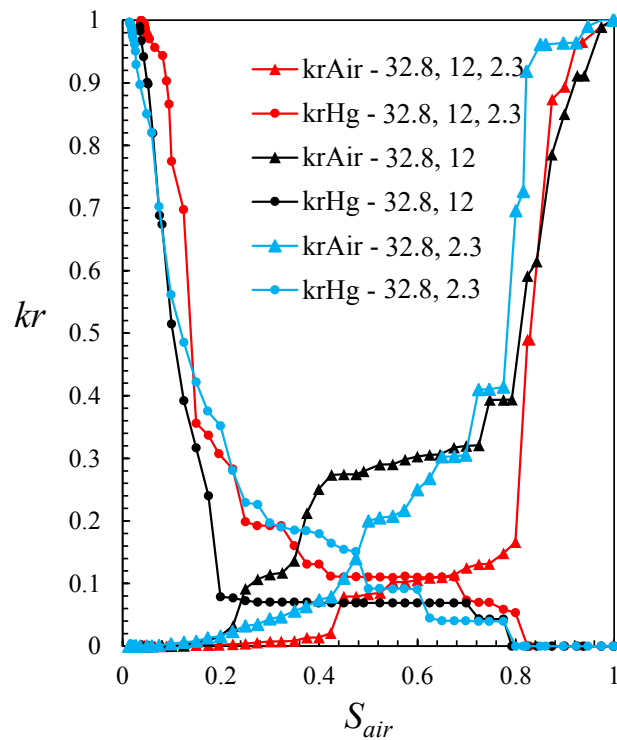


Figure S5: $kr(S)$ curves are calculated for a drainage process, mercury invading a fully air saturated network.

One important parameter to study on relative permeability curves is the saturation where the non-wetting phase (here mercury) breaks through, i.e. the saturation where $kr_{nw}(S) > 0$. The two-scale network models appear to have very close breakthrough saturations ($S_{air} \sim 0.8$) while the three-scale network displays a slightly earlier breakthrough ($S_{air} \sim 0.82$). This is probably due to the higher average coordination number (3.44) of the three-scale network compared to that of the two-scale network (~ 3) (Table 2). Coordination number is defined as the number of pore-throats connected to each pore. The irreducible air saturation mostly reflects the proportion of the isolated pores present in each network, which are small

This work suggests that the parameters involved in the network integration, as well as the number and resolution of the input single-scale networks, can have a substantial impact on the shape of the $kr(S)$ curves calculated based on the multi-scale network models. As suggested by *Prodanović et al. [2015]* the saturation of the cross-over point displays considerable shifts for different multi-scale pore-networks discussed in this study.